Chapter 1
Hurricane Precipitation Observed by SAR

D.G. Long and C. Nie

Abstract The SAR-observed backscatter from the ocean's surface is related to the surface wave spectrum, which is in turn related to the near-surface vector wind. This enables retrieval of near-surface winds from SAR images. Rain impacting the surface affects the wind-driven surface wave spectrum and roughens the surface. Rain can be observed in SAR images due to the effects the rain has on the surface and scattering and attenuation of the radar signal by the falling rain. With its high resolution SAR is a useful sensor for studying rain. This Chapter focuses on SAR observation of rain in ocean images. The effect of rain on the SAR backscatter image is modeled. Using a case study of RADARSAT ScanSAR SWA images of Hurricane Katrina, rain effects are analyzed for three different incidence angle ranges using collocated ground-based Doppler weather radar (NEXRAD) rain measurements. The rain-induced backscatter observed by the ScanSAR is consistent with C-band scatterometer-derived wind/rain scattering models when the polarization difference between the sensors are considered. New insights into the temporal behavior of rain effects on the small-scale surface wave spectrum derived from the ScanSAR images are presented.

1.1 Introduction

Synthetic aperture radar (SAR) measurements have been used to study coastal processes, currents, and sea ice with its high spatial resolution and large spatial coverage. Studies confirm that SAR measurements can be used in the retrieval of the near ocean surface winds at ultra high resolution [1]. The normalized radar cross section (σ°) measured by microwave radars over the ocean is mainly from wind-driven gravity-capillary waves due to Bragg scattering. By making multiple near

D.G. Long (✉)
Department of Electrical and Computer Engineering, Brigham Young University,
459 Clyde Building, Provo, UT 84602, USA
e-mail: long@ee.byu.edu

C. Nie
Formerly with Department of Electrical and Computer Engineering,
Brigham Young University, 459 Clyde Building, Provo, UT 84602, USA

X. Li (ed.), *Hurricane Monitoring With Spaceborne Synthetic Aperture Radar*, Springer Natural Hazards, DOI 10.1007/978-981-10-2893-9_1

simultaneous observations of the surface backscatter from different azimuth and/or incidence angles at each point in the observation swath, wind scatterometers such as the European Space Agency (ESA) Earth Remote Sensing (ERS) scatterometer (ESCAT), the ESA Advanced Scatterometer (ASCAT), and the U.S. QuikSCAT employ a geophysical model function to estimate the wind speed and direction over the ocean [2–4]. Since SARs have only one measurement for each geographic location, the wind direction must be inferred from the orientation of the wind-induced streaks visible in most SAR images [1, 5, 6], or obtained from additional information such as numerical wind prediction models [7]. Given the wind direction, the wind speed is retrieved from either the spectral width of the image spectrum in azimuth direction or by inversion of a geophysical model function (GMF) that relates the normalized radar backscatter (denoted σ°) to the wind speed and direction. The GMF is a function of the radar frequency, polarization, incidence angle, and azimuth angle and is used by wind scatterometers as well.

Compared with C-band wind scatterometers, SAR can provide wind estimates at much finer (100–1000 m compared to 25 km) resolution, which is useful for studying micro-scale weather events, including rain. Rain cells are often observed in SAR images over the ocean [8, 9]. Rain-induced backscatter is from two processes: atmospheric attenuation and scattering by falling rain drops. The former is small at C-band; however, rain-induced surface scattering can be significant [10]. Raindrops striking the water and downdraft created by rain cells modify the roughness of the ocean surface; and hence the surface backscatter.

Melsheimer et al. [8] analyzed SAR signatures of rain cells over the ocean using C and X-band SAR data, showing that rain generally reduces the surface backscatter at low incidence angles and enhances the backscatter at high incidence angles. Weinman et al. [11] studied rain over the ocean with dual frequency SAR and derived the differential polarized phase shift. Unfortunately, this technique cannot be used with single frequency SAR systems.

Wind and rain retrieval from radar measurements is well-developed in the scatterometer community. For example, using C-band scatterometer measurements Nie and Long [10] found that rain surface backscatter can dominate the total backscatter from the ocean surface in moderate to heavy rains. While rain can degrade the accuracy of scatterometer wind measurements [10, 12], incorporating rain effects into the GMF permits simultaneous retrieval of both wind and rain at Ku-band [13–15] and at C-band [16].

In this study, we consider the effects of rain on Canadian RADARSAT scanning SAR (ScanSAR) wide A (SWA) mode images and present a case study of rain observation during Hurricane Katrina in 2005. In this mode, the image resolution is fairly coarse (500 m), which precludes wind direction estimation from the SAR image. We thus adopt a wind scatterometer-like approach based on Nie and Long [16] to simultaneously infer wind and rain where wind directions are specified with the aid of a hurricane model [7, 17]. Various rain effects in the SAR images are illustrated and analyzed. The high resolution and rapid storm movement permits us to examine a number of short-time temporal effects of the rain on the surface roughness spectrum.

This analysis requires a wind/rain GMF. Lacking a well-validated GMF model for HH polarization at C-band, we adjust the C-band VV polarization scatterometer GMF (CMOD5) [18] using a polarization ratio correction as described in Nie and Long [7].

1.2 Rain Effects on C-Band SAR Measurements over the Ocean

In the atmosphere, rain-induced volume-scattering increases the power backscattered toward the SAR, while also attenuating the signal to and from the surface. Raindrops striking the water create various splash products including rings, stalks, and crowns from which the signal scatters. The contribution of each of these splash products to the backscattering varies with incidence angle and polarization. Ring waves are found to be the dominant features for VV-polarization. For HH-polarization, the radar backscatter from non-propagating splash products increases with increasing incidence angles while the radar backscatter from ring waves decreases. These splash products are imposed on the wind-generated wave field. Raindrops impinging on the ocean surface also generate turbulence in the upper water layer which attenuate the short gravity wave spectrum [10]. Using multi-frequency SIR-C/X-SAR data and ERS 1/2 SAR (C band, VV-polarization) data, Melsheimer et al. [8] demonstrate that the modification of the sea surface roughness by falling raindrops mainly depends on the wavelength of water waves. The net effect of the raindrops on the ocean surface is a decrease of the amplitude of water waves which have wavelengths above 10 cm and an increase of the amplitude of water waves with a wavelength below 5 cm. For waves with wavelengths between 5 and 10 cm, rain may increase or decrease the amplitude of the Bragg waves, though the critical transition wavelength at which increase turns to decrease is not well defined [8]. The critical wavelength is believed to depend on rain rate, drop size distribution, wind speed, and the temporal evolution of the rain event.

In addition to surface effects induced by raindrops, the sea surface roughness is also affected by the airflow (downdraft) associated with the rain event and the large scale wind flow, as illustrated in Fig. 1.1. When the downdraft reaches the sea surface, it spreads radially outward as a strong local surface wind that increases the sea surface roughness. Note that the gust front is the outer edge of the downdraft. When the mean ocean surface wind is low, the downdraft is often visible on SAR images over the ocean as a nearly circular bright pattern with a sharp edge [9, 19]. When the ocean surface wind is strong, the airflow pattern is distorted; hence the SAR signature shows both bright and dark areas [20].

Using C-band scatterometer (ERS-1/2 VV-polarization) measurements, Nie and Long [10] quantitatively analyzed the rain surface effects on C-band radar signals at incidence angles higher than 40°. Their study demonstrates that rain surface

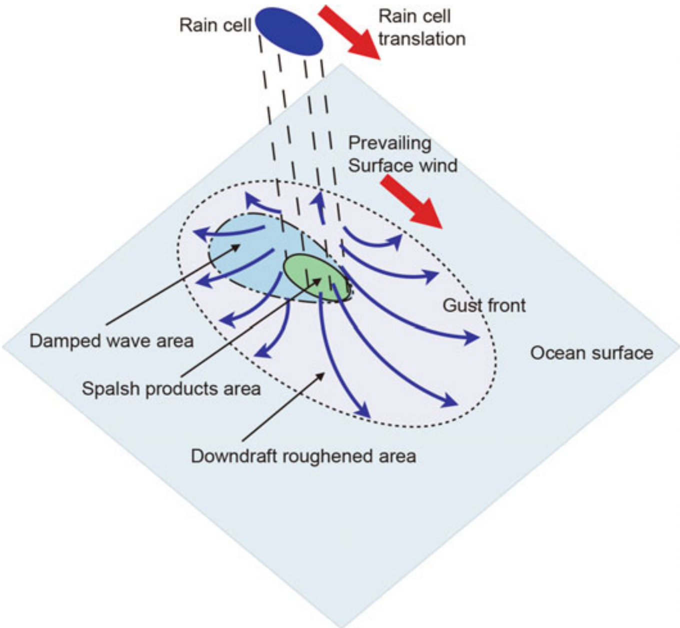

Fig. 1.1 Schematic diagram of the various surface effects caused by a rain cell over the ocean. In the splash area, raindrops striking the water create splash products. The damped wave area is created by rain-generated turbulence in the upper water layer. The *blue arrows* illustrate the airflow of the downdraft, which spreads over and roughens the ocean surface. Note that due to upper atmospheric circulation, the wind cell translates horizontally. In hurricanes, this direction generally coincides with the prevailing surface wind direction

backscatter can dominate the total backscatter in moderate to heavy rains and a simple phenomenological backscatter model can be used to represent rain backscatter with relatively high accuracy. RADARSAT ScanSAR SWA measurements cover wind incidence angle ranges between 20° and 49°, providing a good opportunity to study the effects of rain on C-band HH-polarization SAR measurements at different incidence angles under hurricane conditions. To quantitatively analyze the rain effects on SAR measurements, the wind/rain backscatter model developed in [10] and briefly summarized below is adapted. A SAR response model due to rain atmospheric effects is developed in the following subsections. To estimate SAR wind speed, the recalibration and polarization ratio approach developed by Nie and Long [7] is used. Rain-induced atmospheric attenuation and backscatter are estimated using collocated NEXRAD weather radar data. Finally, rain surface perturbations are estimated and modeled.

1.2.1 Wind/Rain Backscatter Model for SAR

In raining areas, the measured normalized radar cross section by the SAR over the ocean is affected by rain atmospheric effects and various surface effects including splash products, turbulence, and downdraft. As shown in Fig. 1.1, the area affected by downdraft and turbulence is larger than the rain core area. Furthermore, the effect of turbulence varies with the temporal evolution of the rain event at a give location. At the beginning of the rain event, the wave damping effect induced by rain is insignificant because surface turbulence is under development. The dampening grows during the rain event then decays after the rain moves on. Since the turbulence decays slowly due to the molecular viscosity of water and the length scales of the turbulence, the damping effect can exist for some time after a rain event ends [8]. Unfortunately, the lifetime of rain-induced turbulence in water has rarely been studied. As a reference, the lifetime of vortex rings generated by rain drops impinging the water surface is of the order of a minute for a drop diameter of 1 mm [21]. In the analysis of the SAR measurements shown below, the wave damping effect is still observed about five minutes after rain passes and so it is assumed that the lifetime of rain-induced surface turbulence is of this order.

A detailed model of each of the surface effects is beyond the scope of this chapter. Instead, we focus on bulk models for the effects of rain on the Bragg wave field in the rain core area by combining all the surface contributions together into a single rain surface perturbation term, σ_{surf}. σ_{surf} is assumed to be additive with the wind-induced surface backscatter. The rain-modified measured backscatter, σ_m, is represented by a simple additive model [10, 12].

$$\sigma_m = (\sigma_{wind} + \sigma_{surf})\alpha_{atm} + \sigma_{atm} \tag{1.1}$$

where σ_{wind} is the wind-induced surface backscatter, σ_{surf} is the rain-induced surface perturbation backscatter, α_{atm} is the two-way rain-induced atmospheric attenuation, and σ_{atm} is rain-induced atmospheric backscatter.

The σ_{wind} is estimated by projecting H*wind wind speeds (s) and directions (d) through an HH-polarization GMF derived from collocation of H*winds and ScanSAR data [7],

$$\sigma_{wind} = \mathrm{CMOD5}(s, d, \chi, \theta)p(\theta) \tag{1.2}$$

where CMOD5 is the wind-only scatterometer GMF [18], χ is the azimuth angle of SAR measurements, θ is the incidence angle, and $p(\theta)$ is the Thompson et al. [22] polarization ratio model used to convert the VV-pol CMOD5 GMF for use at HH-pol. ScanSAR wind speeds are derived using wind directions from H*wind [7]. Rain-induced atmospheric attenuation and backscatter are estimated using collocated NEXRAD weather radar data.

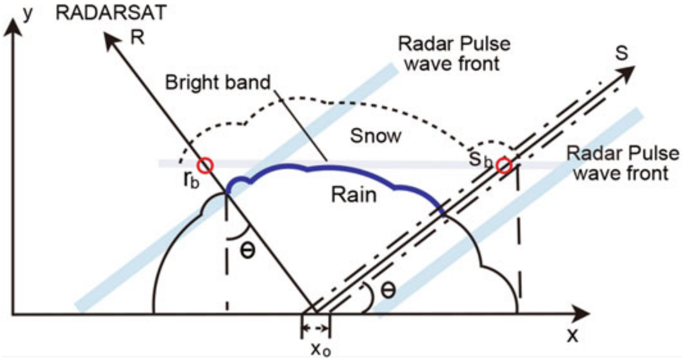

Fig. 1.2 Schematic diagram of the SAR scattering geometry for a rain cell. The *oblique lines* represent the radar pulse under the approximation of plane wave incidence

1.2.2 Evaluation of Atmospheric Attenuation and Backscattering

The SAR measurement geometry is displayed in Fig. 1.2. For simplicity, we use a plane-wave incidence approximation to represent the synthetic aperture radar pulse. We define a new coordinate system $r - s$. r is along the SAR slant range and s is perpendicular to r. For the SAR surface backscatter at $x_{\circ}$, the atmospheric attenuation is contributed by the raindrops along coordinate r from the surface to the bright band altitude and by snow above the bright band. The typical altitude of the bright band is about 5 km.

The attenuation coefficient of rain, K_r, can be estimated using the $k_r - R$ (R is rain rate in mm/h) relationship [23]

$$K_r = aR^b \quad \text{dBkm}^{-1} \tag{1.3}$$

where $a = 0.0018$ dBkm^{-1} and $b = 1.05$ for a 5 cm SAR signal wavelength. R is the rain rate in mm/h. The attenuation coefficient of snow is related to snowfall rate by [23]

$$K_s = 0.0222\frac{R^{1.6}}{\lambda^4} + 0.34\varepsilon_i''\frac{R}{\lambda} \quad \text{dBkm}^{-1} \tag{1.4}$$

where λ is the wavelength, $\varepsilon_i'' \simeq 10^{-3}$ at $-1\,°$C. For $\lambda = 5.6$ cm, $R = 100$ mm/h, $K_s =$ 0.04 dBkm^{-1}, while $K_r = 0.227$ dBkm^{-1} under the same conditions. Therefore, the attenuation due to snow is negligibly small and is ignored in the following analysis. The path integrated attenuation (PIA) in dB is the integration of $K_r(r, s)$ through the R axis ($s = 0$), from the bright band altitude, r_b (shown in Fig. 1.2), to the ocean surface, 0,

$$PIA = 2\int_0^{r_b} k_r(r, 0)dr \quad \text{dB} \tag{1.5}$$

where $k_r(r, 0) = aR(r, 0)^b$. Since $r = (x_0 - x)/\sin\theta$ and $k_r(r, 0) = k_r(x, (x_0 - x)/\tan\theta)$, the above equation can be expressed as

$$PIA = 2\frac{1}{\sin\theta}\int_{x_0 - r_b\sin\theta}^{x_0} k_r\left(x, \frac{x_0 - x}{\tan\theta}\right)dx \quad \text{dB} \tag{1.6}$$

The net two way atmospheric attenuation factor α_{atm} is calculated by converting the PIA from dB to normal space,

$$\alpha_{atm} = 10^{-PIA/10} \tag{1.7}$$

In this study the atmospheric backscatter (σ_{atm}) expected for SAR observations is estimated from the rain rate obtained from the NEXRAD measurements using these expressions. For a specific position on coordinate s, the effective reflectivity of the atmospheric rain, $Z_e(0, s)$, is calculated using Eq. (1.13). The volume backscattering coefficient σ_{vc} can be computed from [23]

$$\sigma_{vc}(0, s) = 10^{-10}\frac{\pi^5}{\lambda_\circ^4}|K_w|^2 Z_e(0, s) \quad \text{m}^2/\text{m}^3 \tag{1.8}$$

where $\lambda_\circ = 5.6$ cm is the wavelength of RADARSAT SAR, and $|K_w|^2$ is a function of the wavelength $\lambda_\circ$ and the physical temperature of the material. K_w is assumed to be 0.93 for the water and 0.19 for snow in this paper [24]. The quantity σ_{vc} represents physically the backscattering cross-section (m^2) per unit volume (m^3). According to Fujiyoshi et al. [25], the Z-R relationship for snow is $Z = 427R^{1.09}$. As previously noted, due to its small contribution snow-induced volume backscattering is disregarded in this study.

The volume backscattering cross-section observed by the SAR is attenuated by the two-way attenuation factor, $\alpha_{atm}(0, s)$,

$$\sigma_{vro}(0, s) = \sigma_{vc}(0, s)\alpha_{atm}(0, s) \tag{1.9}$$

where $\alpha_{atm}(0, s)$ is the path integrated two-way attenuation at s on S axis. The total atmospheric rain backscatter as seen by SAR is $\sigma_{vro}(r, s)$ integrated through the radar pulse plane (along the S axis where $r = 0$) from the bright band altitude on the S axis (shown in Fig. 1.2), s_b, to the ocean surface,

$$\sigma_{atm} = \sin\theta\int_0^{s_b}\sigma_{vro}(0, s)ds \quad \text{m}^2/\text{m}^2 \tag{1.10}$$

where θ is the incidence angle. Since $s = (x - x_0)/\cos\theta$ and $\sigma_{vro}(0, s) = \sigma_{vro}(x, (x - x_0)\tan\theta)$, this equation can be transformed to coordinate $x - y$ as

$$\sigma_{atm} = \tan\theta\int_{x_0}^{x_0 + s_b\cos\theta}\sigma_{vro}\left(x, (x - x_0)\tan\theta\right)dx \tag{1.11}$$

After calculating σ_{atm} and α_{atm}, we estimate the surface perturbation backscatter σ_{surf} by

$$\sigma_{surf} = \alpha_{atm}^{-1}(\sigma_m - \sigma_{atm}) - \sigma_{wind} \tag{1.12}$$

where the σ_{surf} can be negative at low incidence angles, corresponding to the loss of the wind-induced backscatter. A positive value is an increase in the net backscatter.

1.3 Data

Hurricane Katrina attained Category 5 status on the morning of August 28 and reached its peak strength at 1:00 p.m. that day. At approximately midnight of August 28, 2007, RADARSAT flew over Katrina, providing an excellent wide swath set of C-band measurements in a hurricane. During the same period, shore-based NEXRAD and air-borne NOAA WP-3D radar also covered Hurricane Katrina from different locations, acquiring 3 dimensional rain. In this section, the data sets used in this study are briefly described. In Fig. 1.3, we show the path of Hurricane Katrina, the outlines of the RADARSAT ScanSAR SWA data, the locations of NEXRAD weather radar stations and the path of the NOAA WP-3D.

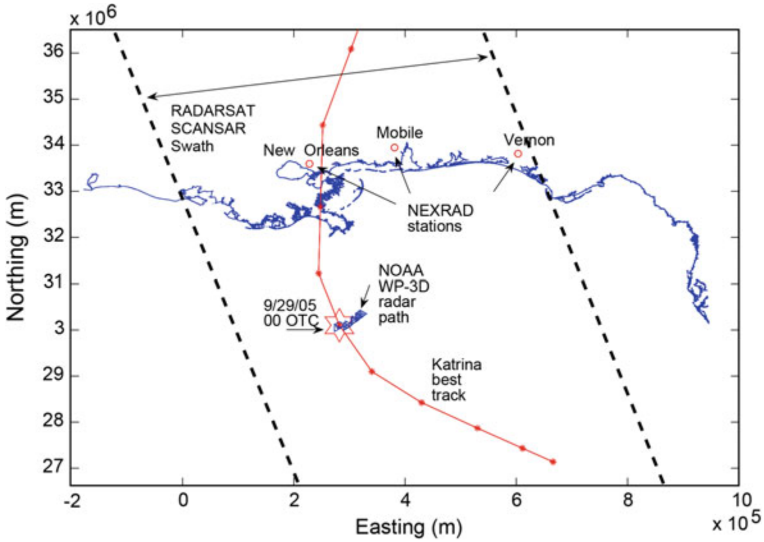

Fig. 1.3 Diagram of the Hurricane Katrina best track as determined by the Hurricane Research Division, the RADARSAT ScanSAR SWA observation swath, and the path of the NOAA WP-3D airplane. Three NEXRAD weather radar stations are plotted as *red circles*. The large star shows the Katrina eye center location at the time of the RADARSAT overpass

1.3.1 RADARSAT ScanSAR SWA Data

The Canadian satellite RADARSAT works at 5.3 GHz in HH polarization. The scanning SAR (ScanSAR) wide A (SWA) mode of RADARSAT provides coverage of a 500 km nominal ground swath at incidence angles between 20° and 49°, with a spatial resolution of 100 m [26].

Two 510 × 510 km calibrated RADARSAT ScanSAR SWA images were acquired over the ocean around New Orleans at 23:49:05 and 23:50:50, on 28 August, 2005, during the period of Hurricane Katrina. At the time of observation, the hurricane was a Category 5 hurricane with a fully developed eye.

The image processed by the Alaska Satellite Facility (ASF) is 510 × 510 km with a pixel spacing of 50 m. The range resolution of the four beams varies from 73.3 to 162.7 m, while the azimuth resolution varies from 93.1 to 117.5 m. The raw ScanSAR SWA data was processed by the ASF into calibrated images. However, the radiometric calibration of ScanSAR SWA images is very difficult due to many limitations including scalloping between the bands, underestimation of σ° [27], and beam overlapping. It is also noted that the calibration at ASF is mainly "tuned" to high latitude areas, which may result in degraded calibration for low latitude areas. The accuracy of the ASF-calibrated SWA images has not been well studied. In Albright [28], the relative radiometric accuracy for SWA is estimated to be about 0.47 dB. The ScanSAR SWA geographic location accuracy is thought to be similar to the overall relative location error of the ScanSAR SWB, about 135 m.

To retrieve vector winds, the parameters needed for wind retrieval are estimated from the SAR image. The incidence angle for each image pixel is calculated from ScanSAR SWA data using a method proposed by Shepherd [29] and the normalized radar cross section σ° is calculated for each pixel [7].

In the two ScanSAR images, rain bands exist next to the eyewall of Katrina and several long rain cell clusters span a wide range of incidence angles, providing a good data source to study rain effects on measurements at various incidence angles.

1.3.2 Hurricane Research Division H*wind Data

To validate the SAR retrieved wind fields and calculate the wind-induced backscatter, coincident H*wind surface wind fields [30] are used in the study. The H*wind Surface Wind Analysis System is an experimental high resolution hurricane research tool developed by the Hurricane Research Division (HRD) at the National Oceanic and Atmospheric Administration (NOAA). The H*wind system assimilates and synthesizes disparate observations into a consistent wind field. The H*wind system uses all available surface weather observations. All data are processed to conform to a common framework for a 10 m height, the same exposure, and the same averaging period using accepted methods from micrometeorology and wind engineering [31]. The analysis provides the maximum sustained 1-min wind speed. Due to the limited coverage of the observations and the smoothing effect of the analysis process, fine scale details of the ocean surface winds are filtered out. The spatial resolution of H*wind estimates is 0.0542° in latitude and longitude, while the time resolution is 3 h. The H*wind-predicted wind fields are trilinearly interpolated in space and time to RADARSAT ScanSAR SWA data times and locations.

1.3.3 NEXRAD Doppler Weather Radar Data

NEXRAD is a collection of ground-based weather radars deployed throughout the U.S. Several NEXRAD stations monitored Hurricane Katrina as it closed in on the coast. NEXRAD observations provide three-dimensional rain rates which we can compare to the SAR-derived rain rates. The NEXRAD radar operates at S-band (2.7–3.0 GHz). During storm events, NEXRAD uses a pre-programmed set of scanning elevations, Volume Coverage Pattern (VCP) 11, to acquire data. The radar successively scans 360° in azimuth angle in 1° increments and from 0.5° to 6.2° in 0.95° increments in elevation angle. Additional circular scans at a 7.5°, 8.7°, 10.0°, 12.0°, 14.0°, 16.7°, and 19.5° elevation angle are performed [32, 33].

In general, rain rates are derived from NEXRAD measurements of reflectivity Z by inversion of the reflectivity to rain rate (Z-R) relationship,

$$Z = aR^b \tag{1.13}$$

where constants a and b are dependent on drop-size distribution. The optimal Z-R constants determined by Jorgensen and Willis [34] in mature hurricanes are $a = 300$ and $b = 1.35$. The NEXRAD Z measurements are estimated at 1 km resolution over the range of 1–460 km from the radar.

To collocate the NEXRAD rain measurements with RADARSAT ScanSAR SWA data, the NEXRAD measurements are converted from Plan Position Indicator (PPI) to Constant Altitude Plan Position Indicator (CAPPI) with 1×1 km resolution in the horizontal and 1 km resolution in the vertical. Interpolation is used to project the measurements from PPI to CAPPI. The ray path is computed using the "four-thirds earth radius model" [35]. The NEXRAD rain rates are then projected to UTM coordinates.

As shown in Fig. 1.3, NEXRAD data from stations at New Orleans (LIX), Mobile (MOB), and Tallahassee (EVX and TLH) are used. In the overlapping area of two radars, we select the rain estimates from the nearest station. To ensure the quality of the rain estimates, we limit the maximum range of NEXRAD radar data to a 200 km radius.

1.4 Results and Analysis

As noted, rain effects vary with incidence angle. In the following we quantitatively analyze the radar backscatter of several rain cells at different incidence angles.

1.4.1 Incidence Angle Between 22° and 23.6°

Figure 1.4 displays the SAR $\sigma°$ of a typical rain cell located near the coast in this dataset. The collocated H*wind speed and vectors are shown in Fig. 1.5. The incidence angles of the SAR measurements are between 22° and 23.6°. At this incidence angle, the dominant rain effect is a dampening of the surface backscatter; hence, the rain cell looks darker than the surrounding rain-free ocean in the SAR image. The H*wind model predicts that the wind speed over the imaged area is essentially constant. Since the LIX NEXRAD station is the closest station to this site, radar data from the LIX station is used to calculate rain rates.

Because the gain spatial response function is not uniform over the NEXRAD footprint, the NEXRAD-observed rain is a weighted spatial average of the rain. To compensate for this, the collocated SAR measurements are averaged over the NEXRAD footprint by weighting with the NEXRAD spatial response function within

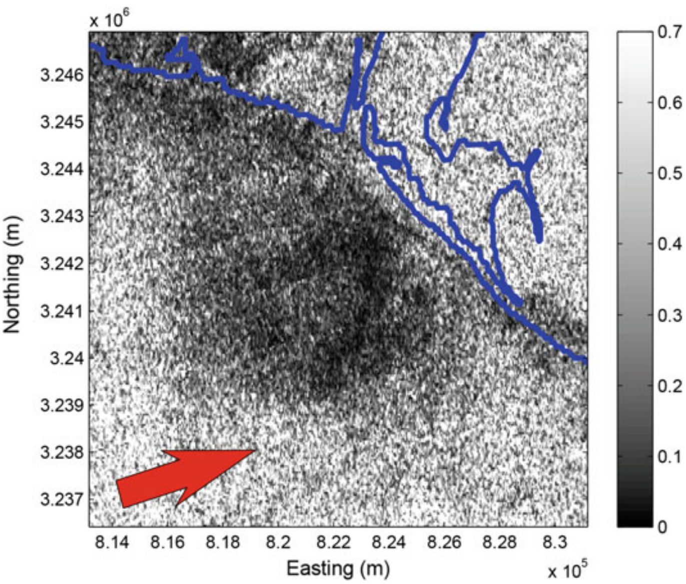

Fig. 1.4 $\sigma°$ of a rain cell located near the sea shore of New Orleans in Hurricane Katrina. The coast line is marked using solid lines and the *red arrow* shows the azimuth direction of RADARSAT ScanSAR observation. The near-surface wind speed is ≈20 m/s

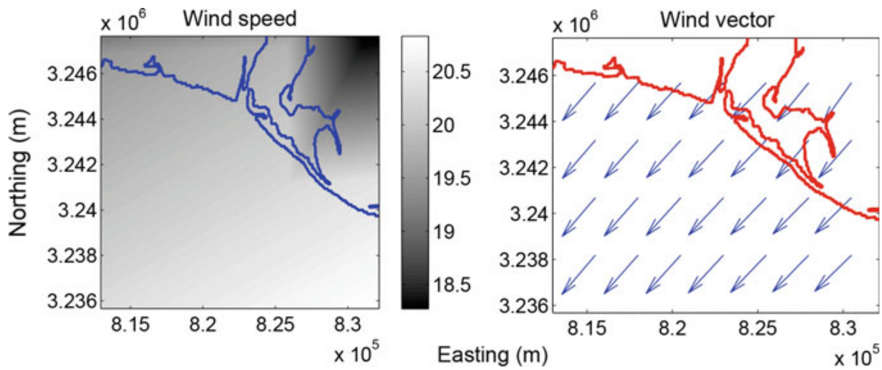

Fig. 1.5 Collocated H*wind winds corresponding to the region in Fig. 1.4

the 3-dB antenna pattern contour. Lacking detailed information for NEXRAD's spatial response function, we use a Gaussian radiation pattern in this study [35]. To minimize the errors introduced by the SAR and NEXRAD data processing, the different map projections, and the spatial and time differences between the two sensors, we assume the rain is uniformly distributed in the vertical direction and use the vertically-averaged rain rate as the surface rain rate. Due to the coarse resolution of the SCANSAR image, we do not attempt to separate atmospheric rain from the surface rain effects.

Figure 1.6a and b displays the atmospheric attenuation and backscatter induced by rain and computed from NEXRAD observations. Compared with the surface σ° at this incidence angle range, the atmospheric backscatter is insignificant, while the atmospheric attenuation is significant in heavy rains. Due to the SAR geometry, the SAR measurements affected by rain atmospheric attenuation and backscattering are not limited to the rain-cell area. Figure 1.7a and b display the collocated σ_{surf} and the NEXRAD surface rain rate, respectively. In Fig. 1.7c and d, the profiles of rain rate and σ_{surf} are plotted along the red solid line in Fig. 1.7a and b. These show that the σ_{surf} generally decreases as rain rate increases. Note that the profile of σ_{surf} is wider than the rain rate profile.

To relate the σ_{surf} with rain rate, we use a power law model [10]. σ_{surf} can be expressed as a polynomial function of rain rate,

$$10log_{10}(\sigma_{surf}(\theta)) \approx f_{sr}(R_{dB}) = \sum_{n=0}^{N} x_{sr}(n) R_{dB}^{n} \qquad (1.14)$$

where $R_{dB} = 10log_{10}(R_{surf(ant)})$, and $x_{sr}(n)$ are the corresponding model coefficients. $N = 1$ for the linear model, and $N = 2$ for the quadratic model. Because the estimate of σ_{surf} is relatively noisy, we first make a nonparametric estimate of σ_{surf} as a function of R_{dB} using an Epanechnikov kernel with a 2 mm/h dB bandwidth in rain rate as shown in Fig. 1.8a. Then, we estimate the model coefficients for the

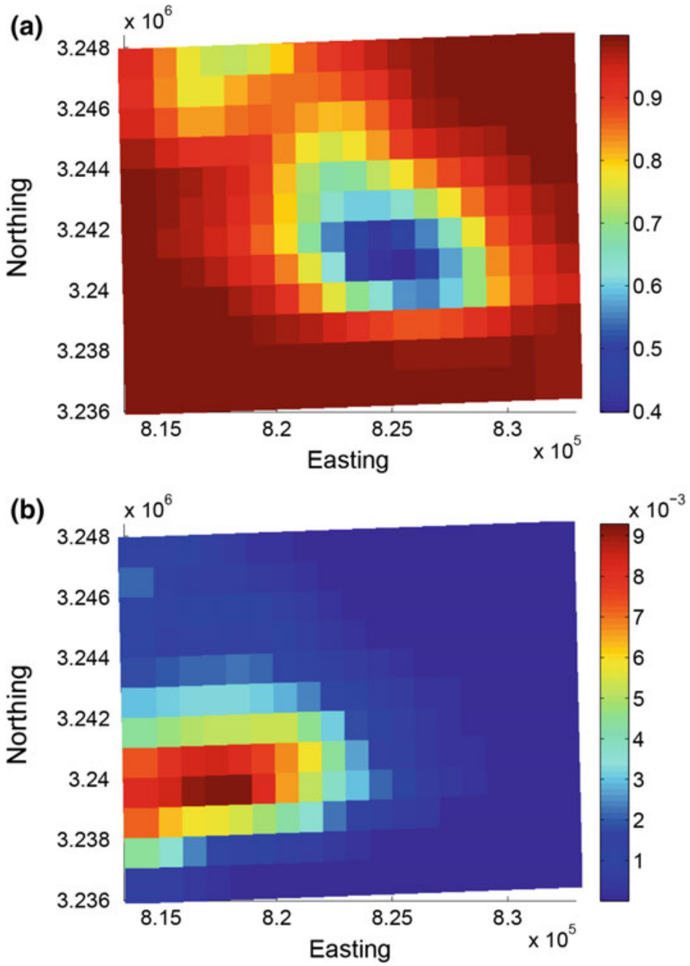

Fig. 1.6 **a** Rain-induced atmospheric attenuation and **b** atmospheric backscatter computed from NEXRAD observations over the region in Fig. 1.4

quadratic model using a linear least-squares fit as shown in Fig. 1.8b. In the following analysis of other rain cells, we use this same method. With the estimated model coefficients it is possible to infer the rain rate from the SAR-derived σ_{surf}.

1.4.2 Incidence Angle Between 28° and 31.7°

Figure 1.9 displays the SAR signature of a rain cell over the ocean about 150 km from the MOB NEXRAD station. Figure 1.10 displays the collocated H*wind speeds and

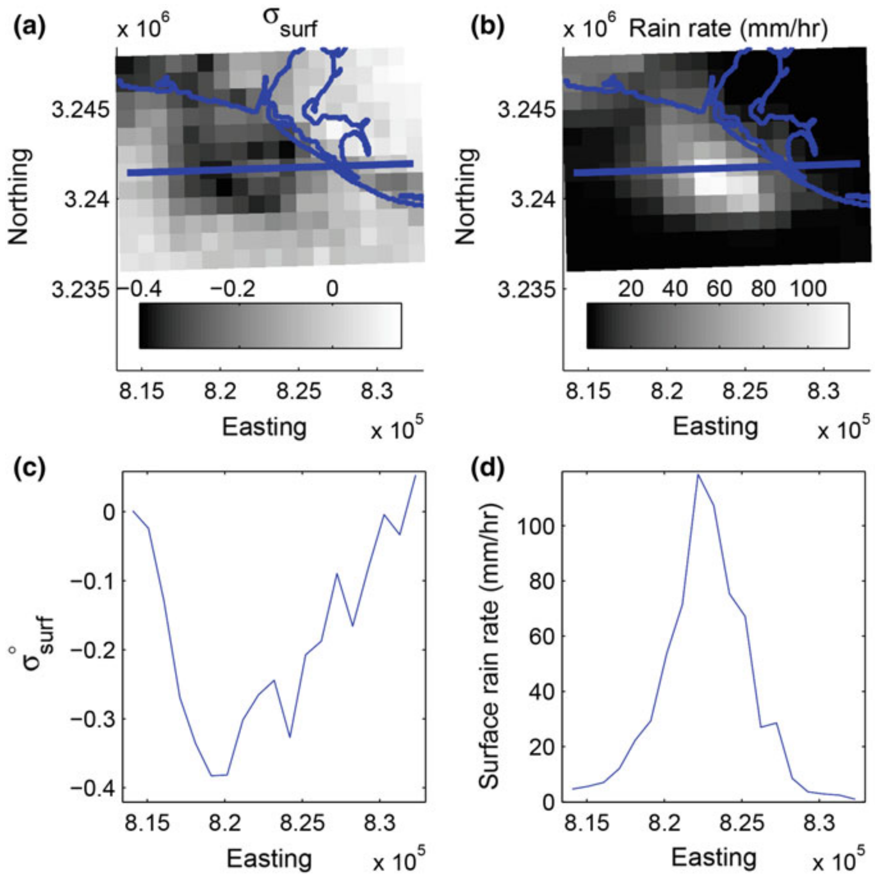

Fig. 1.7 **a** σ°_{surf} surf of the rain cell in Fig. 1.4. **b** The collocated NEXRAD rain rate in mm/h. **c** and **d** the profile of σ° and rain rate along the *solid line* plotted in **a** and **b**

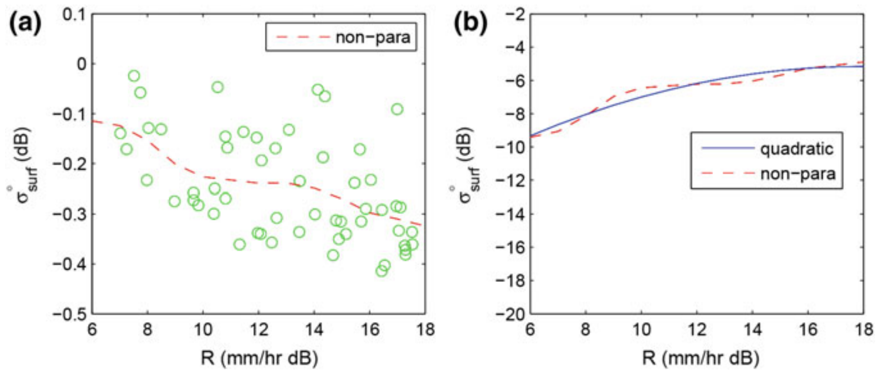

Fig. 1.8 **a** σ°_{surf} versus rain rate nonparametric fit. **b** Quadratic fit to σ_{surf} in log-log space compared to the non-parametric fit

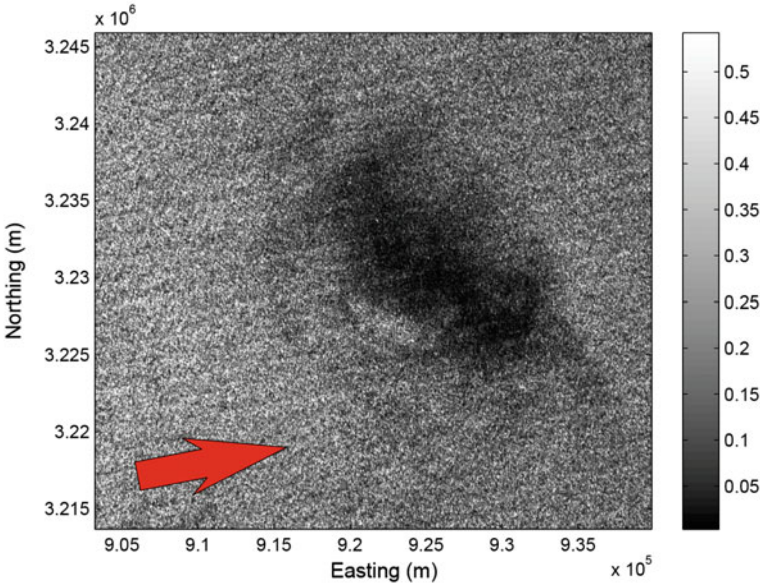

Fig. 1.9 RADARSAT $\sigma°$ of a rain cell located near the sea shore of New Orleans in Hurricane Katrina. The *red arrow* shows the azimuth direction of RADARSAT ScanSAR observation. The near-surface wind speed is ≈22 m/s

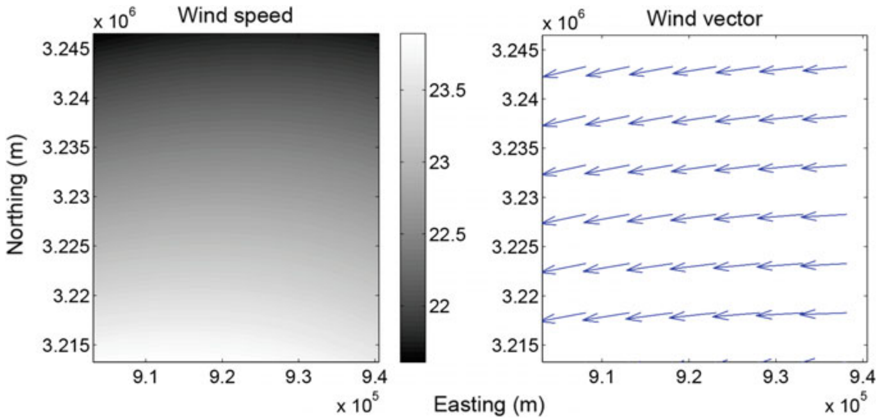

Fig. 1.10 Collocated H*wind winds corresponding to the region in Fig. 1.9

directions. At this SAR incidence angle range, the damping effect of the rain on the surface wave spectrum is dominant. Figure 1.11 analyzes the normalized radar cross-section of this event. The collocated NEXRAD-derived rain rate of the intense rain cell shown in Fig. 1.11b creates the spatially larger SAR signature illustrated in Fig. 1.11a. The rain effect depresses the surface backscatter creating an apparent

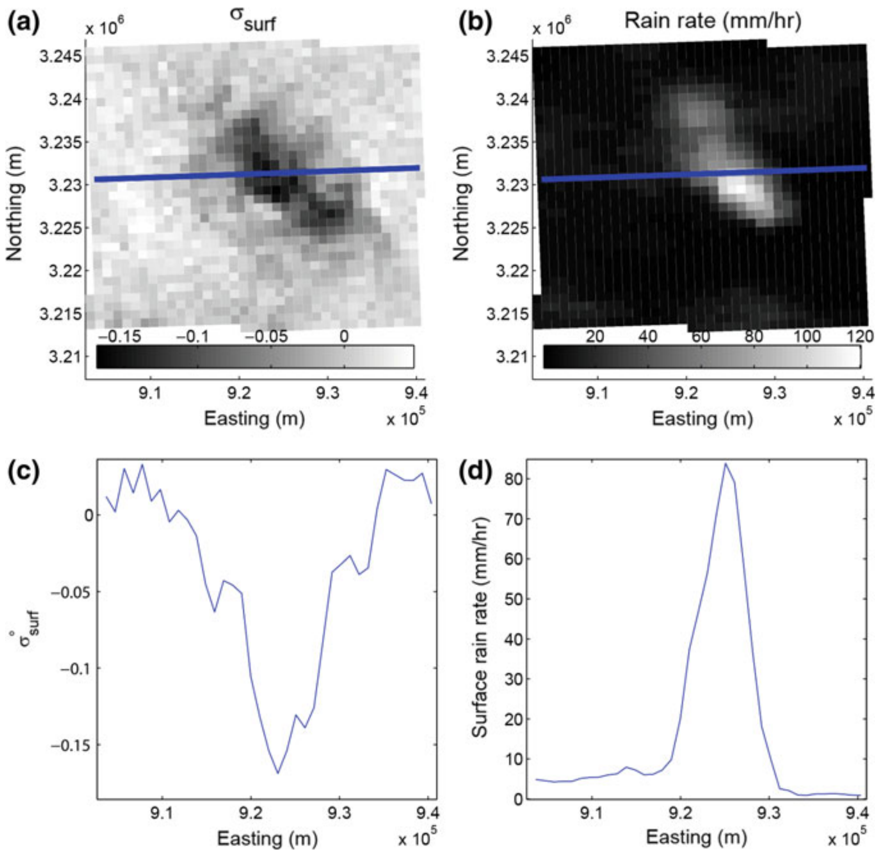

Fig. 1.11 **a** σ°_{surf} of the rain cell in Fig. 1.9. **b** The collocated NEXRAD rain rate in mm/h. **c** and **d** the profile of σ° and rain rate along the *solid line* plotted in **a** and **b**

negative "surface backscatter". As shown in Fig. 1.12, the loss due to the damping effect is as high as -7 dB when $R \approx 63$ mm/h, which is significant compared to the wind-induced surface backscatter. Figure 1.12a illustrates the non-parametric fit to the estimated σ_{surf} derived from the SAR data with respect to R_{dB} while (b) displays the quadratic fit to the non-parametric fit. Due to the relatively large number of collocated data points, the nonparametric fit in Fig. 1.12a is smooth and the quadratic fit agrees well with the nonparametric fit in Fig. 1.12b.

1.4.3 Incidence Angle Between 44° and 45.7°

Figure 1.13 displays the SAR signature of a rain cell over the ocean which is about 70 km from the EVX NEXRAD station. Through comparison between σ_{surf} and rain

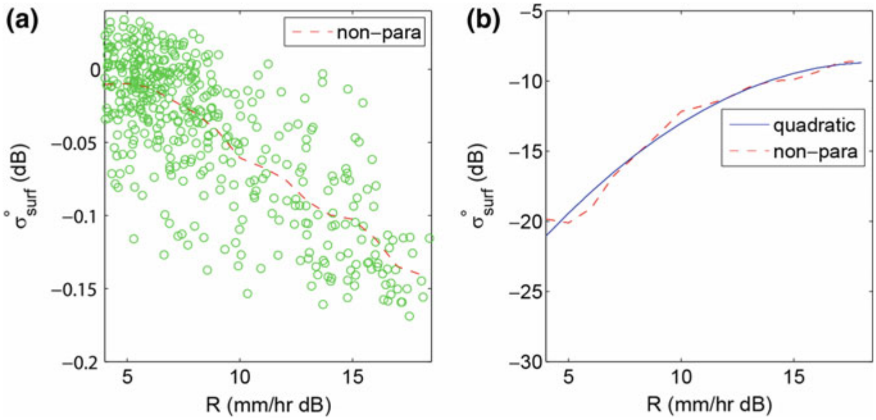

Fig. 1.12 **a** Nonparametric fit to σ_{surf}. **b** Quadratic fit to the non-parametric fit of σ_{surf} in log-log space

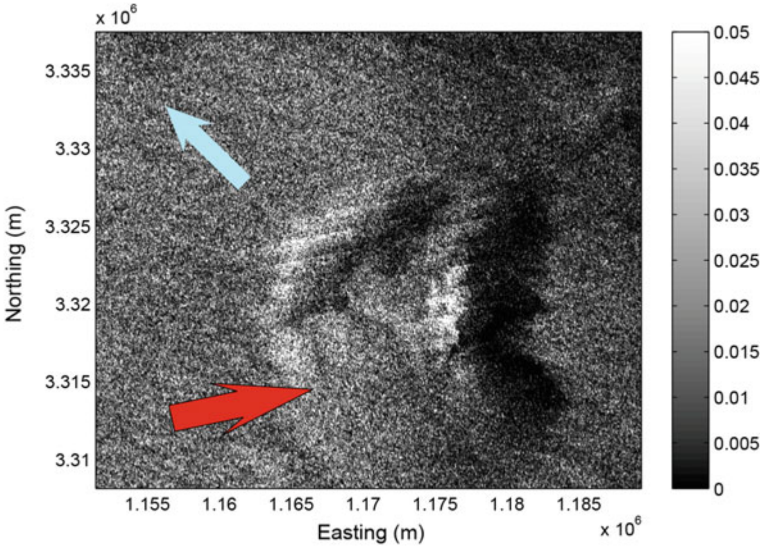

Fig. 1.13 σ° of a rain cell located near the sea shore of New Orleans in Hurricane Katrina. The *red arrow* shows the azimuth direction of RADARSAT ScanSAR observation and the light *blue arrow* shows the wind direction. The near-surface wind speed is $\approx$10 m/s

rate in Fig. 1.15, we find that the enhancing effect of rain is dominant within the rain cells. However, damping areas (which are darker due to reduced σ°) are found next to the rain enhanced areas. The damping areas have shapes similar to the rain cells but are shifted due to the motion of the rain cell. Note that two negative peaks exist in the profile of σ_{surf} along the solid line, as shown in Fig. 1.15. Because the wind direction is pointing in the west-northern direction, as shown in Fig. 1.14, the rain

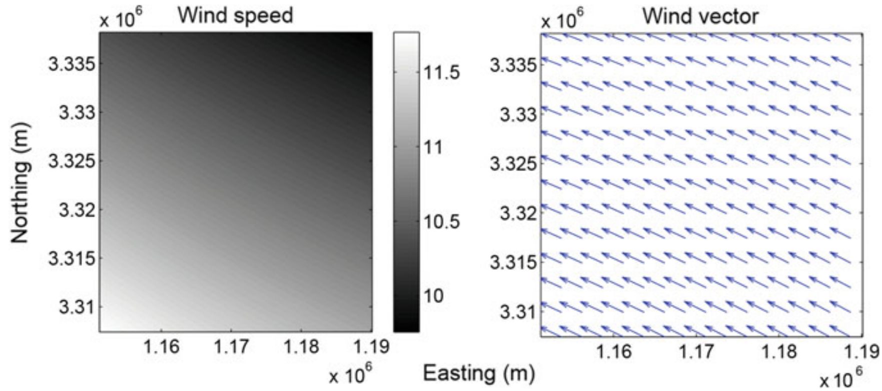

Fig. 1.14 Collocated H*wind winds corresponding to the region in Fig. 1.13

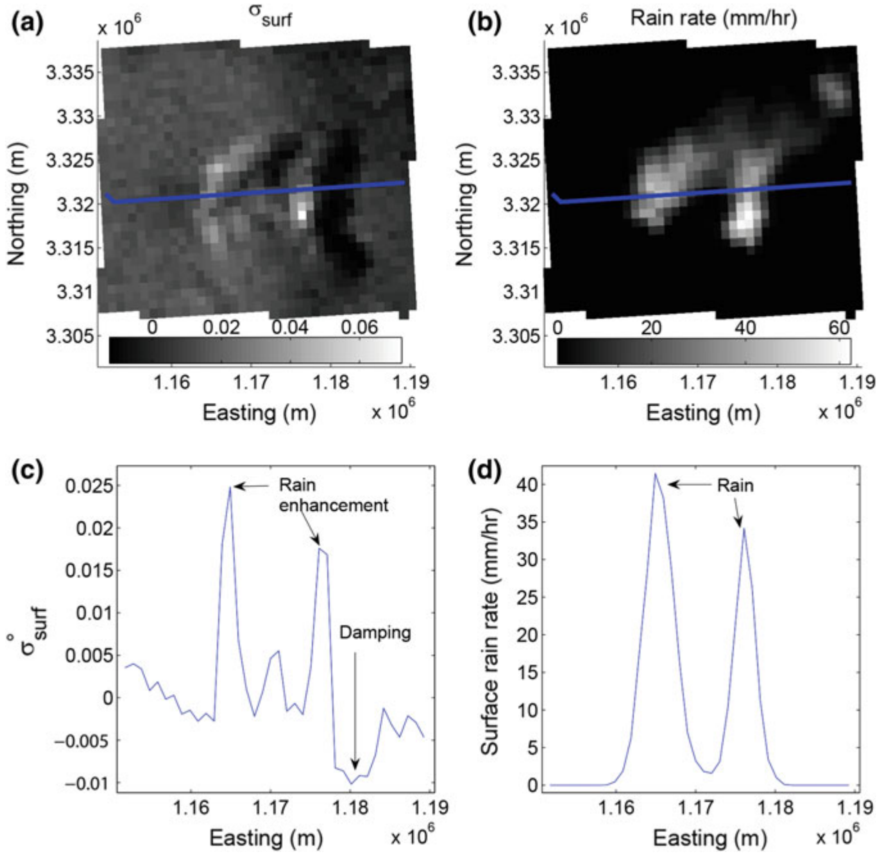

Fig. 1.15 **a** σ°_{surf} of the rain cell in Fig. 1.13. **b** the collocated NEXRAD rain rate in mm/h. **c** and **d** display the profile of σ° and rain rate along the *solid line* plotted in **a** and **b**

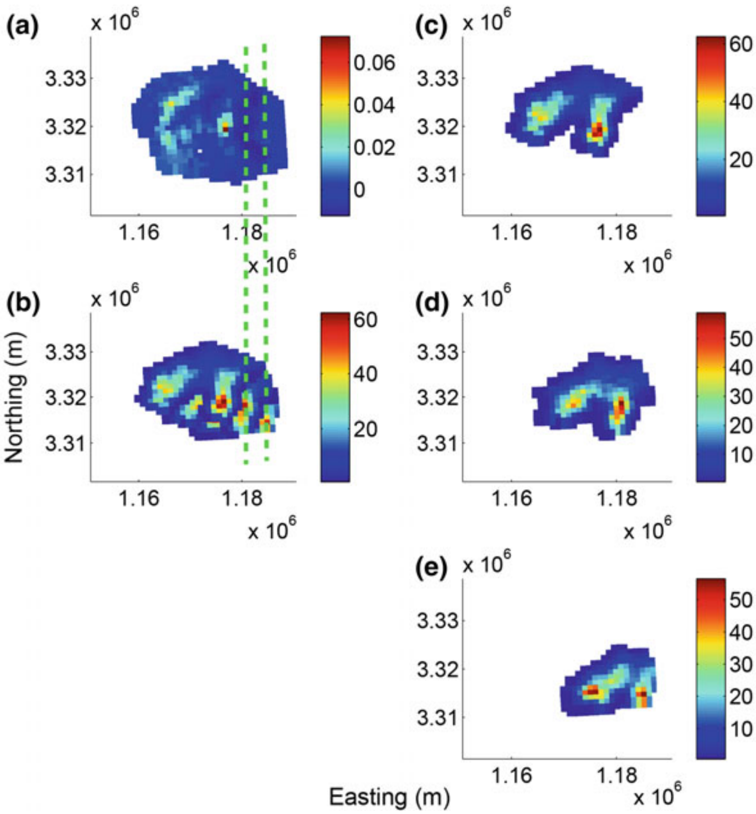

Fig. 1.16 **a** σ_{surf} derived from the RADARSAT image. **b** Overlay of the NEXRAD measurements from **c**–**e**. **c** NEXRAD measurements collocated with the SAR measurement time. **d** NEXRAD measurements about 5 min prior to the SAR observation. **e** NEXRAD measurements about 10 min prior to the SAR observation. The rain cell is moving to the upper left, see Fig. 1.13

cell is moving towards west-north, as shown in Fig. 1.16. The path of the rain cell shown in Fig. 1.16b matches the damping areas shown in Fig. 1.16a. As discussed previously, the damping effect continues after rain events. Hence, the damping area is the result of the rain previously falling in the area. Since the rain cell is moving with the wind, it is leaving a “trail” of damped wave surface, which takes time to “recover”.

We note that the lifetime of the rain damping effect has rarely been studied. It is likely that the lifetime depends on many factors such as the type of rain, rain rate, drop size distribution, wind speed, incidence angle, and so on. However, we can infer the lifetime for these particular SAR observation conditions. As shown in Fig. 1.16a and b, the damping area (near Easting 1.18×10^6 m) collocates with the rain measurements acquired 5 and 10 min previously. Based on this, we conclude that the lifetime of the rain damping effect at C-band is approximately between 5 and 10 min

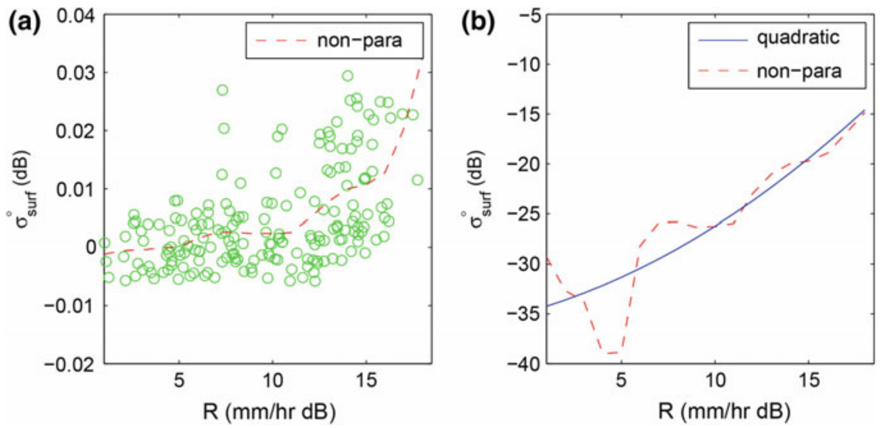

Fig. 1.17 **a** Nonparametric fit to σ_{surf} for Fig. 1.13. **b** Quadratic and linear fits to the non-parametric fits of σ_{surf} in log-log space. Non-parametric fits are also plotted

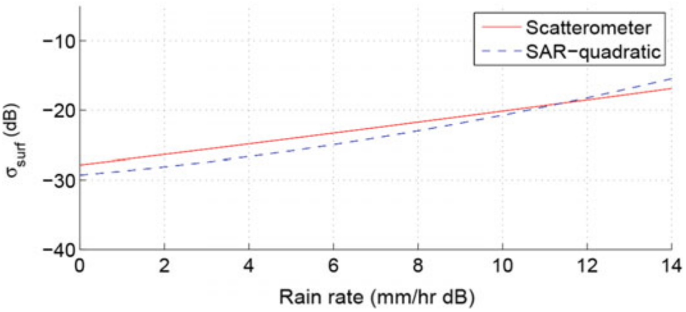

Fig. 1.18 Comparison of SAR-derived and scatterometer-derived surface perturbation, σ_{surf}, versus rain models for VV polarization (see text)

when the wind speed is about 10 m/s, the rain rate is 70 mm/h, and the incidence angle is 45°. This is potentially an important insight into rain/wave interaction.

Figure 1.17a illustrates the non-parametric fit to the estimated σ_{surf} with respect to R_{dB} for this case, while Fig. 1.17b displays the quadratic and linear fits to the non-parametric fit. In Fig. 1.17b, the linear and quadratic model are close, suggesting that σ_{surf} is almost a linear function of surface rain rate in log-log space at this incidence angle. Figure 1.18 compares the scatterometer C-band VV polarization wind backscatter model developed by Nie and Long [10] and the quadratic model derived from the HH polarization SAR measurements for this case. The latter has been adjusted using the Thompson et al. [22] polarization model to VV polarization. The two rain models are close, suggesting that the SAR-derived σ_{surf} versus rain is consistent with the scatterometer derived model when the polarization difference between HH and VV polarizations is considered. Unfortunately, the limited data preclude a systematic comparison of the two models.

Table 1.1 Coefficients of the σ_{surf} model at three incidence angles

Incidence angle (°)	P(0)	P(1)	P(2)
22–23	−14.6081	1.0563	−0.0295
28–31.7	−28.6799	2.1404	−0.0572
44–45.7	−34.79	0.5249	0.0332

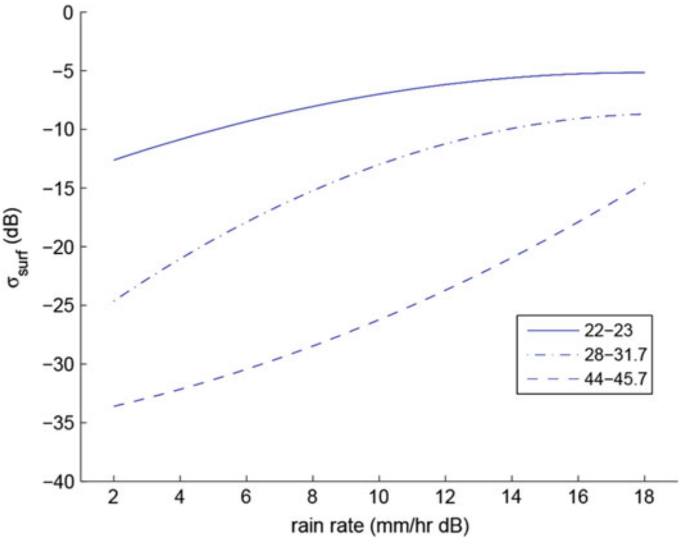

Fig. 1.19 σ_{surf} versus rain rate at different incidence angles. Note that for incidence angle bins 22°–23° and 28°–31° σ_{surf} is negative due to the damping effect. In this case $|\sigma_{surf}|$ in dB is displayed

1.4.4 Rain Model Coefficients

The coefficients of the rain backscatter model for the three incidence angles considered in the previous case studies are listed in Table 1.1. σ_{surf} versus rain rate at the different incidence angles is plotted in Fig. 1.19. The σ_{surf} versus rain model at high incidence angle is close to a linear model in log-log space. Here, we further investigate the relationship between σ_{surf} and incidence angle by plotting the σ_{surf} with respect to incidence angle for a specific surface rain rate in Fig. 1.20. The magnitude of σ_{surf} generally decreases with incidence angles. At heavy rain rates, the decreasing ratio is smaller than at low to moderate rain rates.

At low incidence angles, loss of σ_{surf} occurs due to the damping effect of rain, while rain enhances the backscatter at high incidence angles. As shown in Fig. 1.20, both the loss and enhancement of σ_{surf} can be a significant component of the total backscatter in moderate to heavy rain rates. At extreme rain rates, the wind component of the backscatter may not be significant [16]. Hence, including the rain effects on

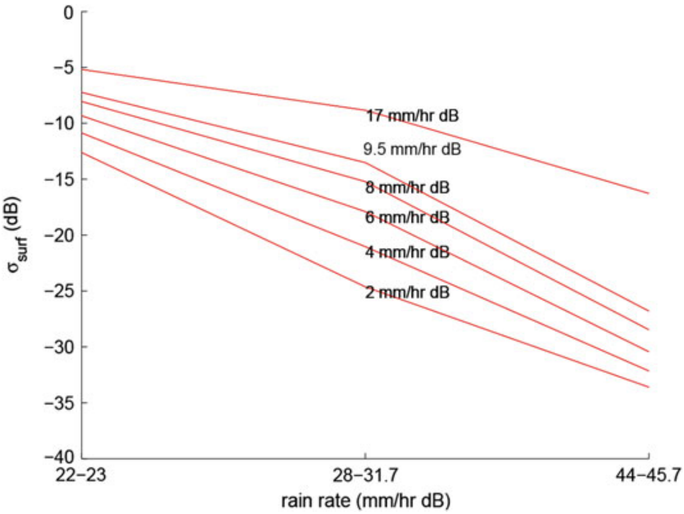

Fig. 1.20 σ_{surf} versus incidence angle for various rain rates at different incidence angles. Note that for incidence angle bins 22°–23° and 28°–31° σ_{surf} is negative due to the rain damping effect. In this case $|\sigma_{surf}|$ in dB is displayed

C-band radar backscatter is very important when attempting SAR wind retrieval in the presence of rain. This is consistent with the wind scatterometer results of Nie and Long [16].

1.5 Conclusion

Rain is clearly visible in C-band RADARSAT ScanSAR SWA images of Hurricane Katrina due to its impact on the radar signal. These include atmospheric effects (attenuation and backscattering) and surface effects. Using a simple wind/rain backscatter model and collocated SAR and NEXRAD data, we quantitatively analyze different rain effects on the ScanSAR measurements for three different incidence angle ranges and estimate the coefficients of a rain GMF. The observed rain signature varies with the incidence angle of the observations. The C-band SAR-derived σ_{surf} is found to be consistent with C-band wind scatterometer-derived models. Rain surface effects on C-band SAR measurements can dominate the surface backscatter in moderate to heavy rains and needs to be considered when retrieving near-surface winds from SAR backscatter data. Based on the pattern rain-induced backscatter damping visible in the imagery, we estimate that the C-band Bragg wave spectrum requires 5–10 min after rain termination to be re-established in moderate winds.

References

1. Wackerman, C.C., C.L. Rufenach, R.A. Shuchman, J.A. Johannessen, and K.L. Davidson. 1996. Wind vector retrieval using ERS-1 synthetic aperture radar imagery. *IEEE Transactions on Geoscience and Remote Sensing* 34 (6): 1343–1352.
2. Attema, E.P.W. 1991. The active microwave instrument on-board the ERS-1 satellite. *Proceedings of the IEEE* 79 (6): 791–799.
3. Figasaldaña, J., J.J. Wilson, E. Attema, R. Gelsthorpe, M. Drinkwater, and A. Stoffelen. 2002. The Advanced scatterometer (ASCAT) on the Meteorological Operational (MetOp) platform: A follow on for European wind scatterometers. *Canadian Journal of Remote Sensing* 28 (3): 404–412.
4. Spencer, M.W., C. Wu, and D.G. Long. 1997. Tradeoffs in the design of a spaceborne scanning pencil beam scatterometer: Application to SeaWinds. *IEEE Transactions on Geoscience and Remote Sensing* 35 (1): 115–126.
5. Vachon, P., and F. Dobson. 1996. Validation of wind vector retrieval from ERS-1 SAR images over the ocean. *The Global Atmosphere and Ocean System* 5 (2): 177–187.
6. Lehner, S., J. Horstmann, W. Koch, and W. Rosenthal. 1998. Mesoscale wind measurements using recalibrated ERS SAR images. *Journal of Geophysical Research: Oceans* 103 (C4): 7847–7856.
7. Nie, C., and D.G. Long. 2008a. RADARSAT ScanSAR wind retrieval and rain effects on ScanSAR measurements under hurricane conditions. In *IEEE International Geoscience and Remote Sensing Symposium*, vol. 2, 493–496. IEEE.
8. Melsheimer, C., W. Alpers, and M. Gade. 2001. By the synthetic aperture radar aboard the ERS satellites and by surface-based weather radars. *Journal of Geophysical Research* 106 (C3): 4665–4677.
9. Atlas, D. 1994a. Footprints of storms on the sea: A view from spaceborne synthetic aperture radar. *Journal of Geophysical Research: Oceans* 99 (C4): 7961–7969.
10. Nie, C., and D.G. Long. 2007. A C-band wind/rain backscatter model. *IEEE Transactions on Geoscience and Remote Sensing* 45 (3): 621–631.
11. Weinman, J., F. Marzano, W. Plant, A. Mugnai, and N. Pierdicca. 2009. Rainfall observation from X-band space-borne synthetic aperture radar. *Natural Hazards and Earth System Sciences* 9 (1): 77–84.
12. Draper, D.W., and D.G. Long. 2004a. Evaluating the effect of rain on SeaWinds scatterometer measurements. *Journal of Geophysical Research: Oceans* 109 (C12).
13. Allen, J.R., and D.G. Long. 2005. An analysis of SeaWinds-based rain retrieval in severe weather events. *IEEE Transactions on Geoscience and Remote Sensing* 43 (12): 2870–2878.
14. Draper, D.W., and D.G. Long. 2004b. Simultaneous wind and rain retrieval using SeaWinds data. *IEEE Transactions on Geoscience and Remote Sensing* 42 (7): 1411–1423.
15. Draper, D.W., and D.G. Long. 2004c. Assessing the quality of SeaWinds rain measurements. *IEEE Transactions on Geoscience and Remote Sensing* 42 (7): 1424–1432.
16. Nie, C., and D.G. Long. 2008b. A C-band scatterometer simultaneous wind/rain retrieval method. *IEEE Transactions on Geoscience and Remote Sensing* 46 (11): 3618–3631.
17. Williams, B.A., and D.G. Long. 2008. Estimation of hurricane winds from SeaWinds at ultra-high resolution. *IEEE Transactions on Geoscience and Remote Sensing* 46 (10): 2924–2935.
18. Hersbach, H., A. Stoffelen, and S. De Haan. 2007. An improved C-band scatterometer ocean geophysical model function: CMOD5. *Journal of Geophysical Research: Oceans* 112 (C3).
19. Atlas, D. 1994b. Origin of storm footprints on the sea seen by synthetic aperture radar. *Science* 266: 1364–1366.
20. Mitnik, L.M. 1992. Mesoscale coherent structures in the surface wind field during cold air outbreaks over the far eastern seas from the satellite side looking radar. *La Mer* 30: 297–314.
21. Hallett, J., and L. Christensen. 1984. Splash and penetration of drops in water. *Journal de Recherches Atmospheriques* 18 (4): 225–242.

22. Thompson, D.R., T.M. Elfouhaily, and B. Chapron. 1998. Polarization ratio for microwave backscattering from the ocean surface at low to moderate incidence angles. In *IEEE International Geoscience and Remote Sensing Symposium*, vol. 3, 1671–1673. IEEE.
23. Battan, L.J. 1973. *Radar Observation of the Atmosphere*. Chicago: The University of Chicago.
24. Ulaby, F.T., R.K. Moore, and A.K. Fung. 1982. Microwave remote sensing active and passive, vol. i.
25. Fujiyoshi, Y., T. Endoh, T. Yamada, K. Tsuboki, Y. Tachibana, and G. Wakahama. 1990. Determination of a Z-R relationship for snowfall using a radar and high sensitivity snow gauges. *Journal of Applied Meteorology* 29 (2): 147–152.
26. Raney, R.K., A.P. Luscombe, E. Langham, and S. Ahmed. 1991. RADARSAT. *IEEE International Geoscience and Remote Sensing Symposium* 79 (6): 839–849.
27. Horstmann, J., W. Koch, S. Lehner, and R. Tonboe. 2000. Wind retrieval over the ocean using synthetic aperture radar with C-band HH polarization. *IEEE Transactions on Geoscience and Remote Sensing* 38 (5): 2122–2131.
28. Albright, W. 2004. Calibration report for RADARSAT ScanSAR Wide A on the ScanSAR processor. *Alaska Satellite Facility*.
29. Shepherd, N. 1998. Extraction of beta nought and sigma nought from RADARSAT CDPF products. *Rep. AS97-5001 Rev*, 2.
30. Powell, M.D., S.H. Houston, L.R. Amat, and N. Morisseau-Leroy. 1998. The HRD real-time hurricane wind analysis system. *Journal of Wind Engineering and Industrial Aerodynamics* 77: 53–64.
31. Powell, M.D., S.H. Houston, and T.A. Reinhold. 1996. Hurricane Andrew's landfall in south Florida. Part I: Standardizing measurements for documentation of surface wind fields. *Weather and Forecasting* 11 (3): 304–328.
32. F. C. for Meteorological Services, and S. Research. 1990. Doppler radar meteorological observations, Part B: Doppler radar theory and meteorology. CM-H11B-1990.
33. F. C. for Meteorological Services, and S. Research. 1991. Doppler radar meteorological observations, Part C: WSR-88D products and algorithms. FCM-H11C-1991.
34. Jorgensen, D.P., and P.T. Willis. 1982. A ZR relationship for hurricanes. *Journal of Applied Meteorology* 21 (3): 356–366.
35. Doviak, R.J., and D.S. Zrnic. 1984. *Doppler Radar and Weather Observations*, vol. I. Dublin: Academic press.